arXiv:2608.28425v1 [cs.LG] 28 Aug 2026

Euclidean Fourier Neural Operators

Nathanael Bosch* **Niklas Frederik Schmitz*** **Michael F. Herbst**
Mathematics for Materials Modelling (MatMat)
Institute of Mathematics & Institute of Materials
École Polytechnique Fédérale de Lausanne, 1015 Lausanne, Switzerland
{nathanael.bosch, niklas.schmitz, michael.herbst}@epfl.ch

Abstract

Fourier neural operators (FNOs) provide an efficient framework for learning mappings between function spaces as they are, by construction, independent of the grid resolution at which they are trained and evaluated. However, FNOs are not independent of the periodic domain they are applied to: their discrete spectral weights are indexed by integer Fourier mode numbers, which correspond to physical wavevectors. When applied to a different domain, the same trained weights act at different wavevectors, and the FNO silently represents a different operator. This makes FNOs unsuitable for tasks where transfer across domains is crucial. We propose Euclidean Fourier neural operators (EFNOs) as a domain-independent alternative to FNOs. By parameterizing the spectral kernel as a continuous function of the physical wavevector, the EFNO can learn operators that act consistently across periodic domains of varying shape and size. We evaluate the EFNO on a simple heat equation and on a practically relevant materials science task of learning exchange-correlation potentials across different crystal structures, and demonstrate that the EFNO is able to generalize to unseen grid sizes and domains.

1 Introduction

Fourier neural operators (FNOs) [Li et al., 2021] have been established as an efficient framework for learning mappings between function spaces, with successful applications throughout the physical sciences, including fluid mechanics [Li et al., 2022], weather and climate forecasting [Pathak et al., 2022, Bonev et al., 2023], and seismology [Yang et al., 2021]. A particular strength of FNOs is that they are, by construction, independent of the grid resolution at which they are trained and evaluated. But many physical problems are not tied to a single fixed domain, and the same problem can be posed on domains of varying shape and size. This requires models that can transfer across domains.

FNOs do not natively support such transfer. Their defining *spectral convolution* layer parameterizes a convolution kernel by discrete trainable weights indexed by Fourier mode numbers $m \in \mathbb{Z}^d$, which correspond to physical wavevectors $k_m \in \mathbb{R}^d$ that depend on the periodic domain (see section 2). Thus, when a trained FNO is applied to a different domain, the same weights act at different wavevectors and the FNO silently represents a different operator. Various extensions to FNOs have been proposed, for applications to irregular grids or varying geometries [Li et al., 2023, Liu et al., 2023, Oguadimma et al., 2026] or via continuous parameterizations of the spectral kernel [Xiao et al., 2024, Shi et al., 2026, Shin et al., 2024, Lee et al., 2026], but their spectral layers still operate on Fourier mode indices and thus retain the same domain dependence.

In this paper, we propose *Euclidean Fourier neural operators* (EFNOs). By parameterizing the spectral kernel as a continuous function of the physical wavevectors, EFNOs learn operators in Euclidean space that can be applied consistently across domains. We evaluate the EFNO on a simple

*Equal contribution.

Preprint.

heat equation and on a materials science task that covers crystal structures of varying shape and size, and demonstrate that, in contrast to the FNO, the EFNO is able to learn operators that generalize to unseen grid sizes and domains.

2 Fourier neural operators and their domain dependence

Neural operators are a class of neural networks designed to learn mappings between function spaces. The common blueprint to parameterize a neural operator $\mathcal{G}_\theta : \mathcal{A} \to \mathcal{U}$ uses a sequence of layers

$$\mathcal{G}_\theta := \mathcal{Q} \circ \sigma(\mathcal{W}_T + \mathcal{K}_T) \circ \cdots \circ \sigma(\mathcal{W}_1 + \mathcal{K}_1) \circ \mathcal{P}, \tag{1}$$

with point-wise linear lifting layer $\mathcal{P}$ and projection layer $\mathcal{Q}$, and T hidden layers consisting of a linear channel-wise transformation $\mathcal{W}_t$, nonlocal kernel integral operators $\mathcal{K}_t$ and nonlinear activation function σ [Kovachki et al., 2023]. The parameterization of the nonlocal operator $\mathcal{K}$ is where most neural operator architectures vary (cf. [Kovachki et al., 2023, Section 4]).

Fourier neural operators (FNOs) [Li et al., 2021] model $\mathcal{K}$ as a convolution operator, parameterized in the Fourier domain where its application becomes a point-wise multiplication:

$$(\mathcal{K}v)(x) = \int_{\mathbb{T}^d} \kappa(x-y)v(y)\mathrm{d}y = \sum_{m\in\mathbb{Z}^d, \|m\|_\infty \le M} \widehat{\kappa}_m \, \widehat{v}_m \, e^{ik_m \cdot x}, \tag{2}$$

where $\mathbb{T}^d = \mathbb{R}^d/\mathbb{Z}^d$ is the periodic domain and $\widehat{\kappa}_m$, $\widehat{v}_m$ denote the Fourier coefficients of κ and v at the wavevector $k_m = 2\pi m$, for $m \in \mathbb{Z}^d$. FNOs then parameterize the Fourier coefficients of κ as a lookup table of trainable weights $\widehat{\kappa}_m =: R_m \in \mathbb{C}^{c\times c}$, where c is the number of channels in the hidden representation v, up to a mode cutoff $\|m\|_\infty \le M$.

A particular strength of FNOs is that they are independent of the resolution at which the input-output pairs are discretized, as long as the grid is fine enough to resolve the retained modes, since finer discretization only adds frequencies beyond the cutoff M. However, FNOs are not independent of the choice of the periodic domain: Consider a general periodic domain $D = \mathbb{R}^d/L\mathbb{Z}^d$, specified by its lattice matrix $L \in \mathbb{R}^{d\times d}$ whose columns span the domain. The wavevectors k_m within the Fourier expansion of eq. (2) then depend on the lattice L as

$$k_m = 2\pi L^{-\top} m. \tag{3}$$

Therefore, if one were to apply the same trained FNO on data from two different domains D and D', the learned weights R_m would be applied at different physical wavevectors k_m, and thus the applied operator $\mathcal{K}$ would differ depending on the domain. For physical applications where one wants to learn and apply a common operator across varying domains, this is a severe limitation.

3 Euclidean Fourier neural operators

We propose a simple modification of the FNO that removes the implicit dependence on the choice of periodic domain. Let $\mathcal{K}$ be a translation-invariant linear convolution operator defined in Euclidean space $\mathbb{R}^d$. Such an operator $\mathcal{K}$ is fully characterized by its *symbol* $\widehat{\kappa} : \mathbb{R}^d \to \mathbb{C}^{c\times c}$, by which it acts in Fourier space as $\widehat{(\mathcal{K}v)}(k) = \widehat{\kappa}(k)\,\widehat{v}(k)$ for any $k \in \mathbb{R}^d$. For any given L-periodic function v, the action of $\mathcal{K}$ on v can be expressed in real space as a Fourier series

$$(\mathcal{K}v)(x) = \sum_{m\in\mathbb{Z}^d} \widehat{\kappa}(k_m)\,\widehat{v}_m \, e^{ik_m\cdot x}, \qquad \text{with} \quad k_m = 2\pi L^{-\top} m. \tag{4}$$

Instead of learning a lookup table over mode numbers m, we propose here to directly parameterize the continuous symbol $\widehat{\kappa}_\theta : \mathbb{R}^d \to \mathbb{C}^{c\times c}$, such that it can be evaluated at any wavevector k the domain at hand requires. We call the resulting operator the *Euclidean Fourier neural operator* (EFNO).

In practice, as in the FNO, we assume that the input-output pairs are discretized on uniform grids such that we can use FFTs to efficiently compute $\widehat{v}_m$ and to reconstruct $(\mathcal{K}v)(x)$ on the grid. But additionally, this assumption truncates the Fourier series expansion of eq. (4): If v is discretized on a grid $N_1 \times \cdots \times N_d$, the FFT resolves only modes with $|m_j| \le N_j/2$ for $j = 1, \ldots, d$, turning the series into a finite sum. Thus, unlike the FNO, the EFNO does not require any fixed mode cutoff.

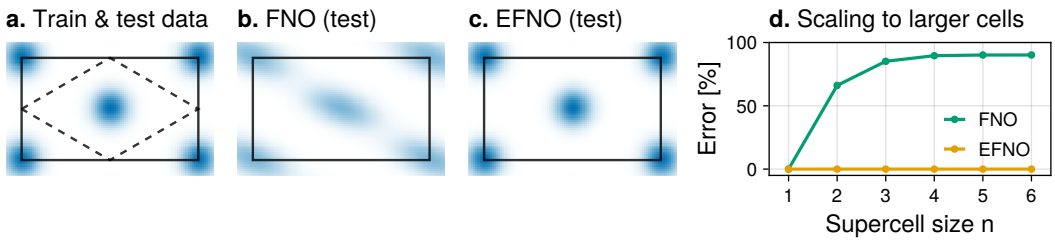

Figure 1: **Domain transfer test for a learned convolution. a**. A periodic array of Gaussian sources, smoothed by the heat kernel. Both models are fitted in the small rhombic cell (dashed), and evaluated on the equivalent rectangular cell (solid). The FNO (**b**.) distorts visibly, while the EFNO (**c.**) transfers perfectly. **d.** Relative L_2 error of the FNO and EFNO on $n \times n$ supercells of the fitting cell. The FNO error grows with the size of the supercell, while the EFNO error remains constant.

Parameterizing the continuous symbol $\widehat{\kappa}_\theta(k)$ also enables the incorporation of physical inductive biases, since known properties of the operator $\mathcal{K}$ translate directly into constraints on $\widehat{\kappa}_\theta$: a smooth real-space kernel $\kappa_\theta(x)$ requires a decaying $\widehat{\kappa}_\theta(k)$; exponential decay in $\kappa_\theta(x)$ requires smoothness in $\widehat{\kappa}_\theta(k)$; $E(3)$-equivariance on scalar channels requires an isotropic symbol $\widehat{\kappa}_\theta(k) = \widehat{\kappa}_\theta(|k|)$; and real-ness of $\kappa_\theta(x)$ requires Hermitian symmetry $\widehat{\kappa}_\theta(-k) = \overline{\widehat{\kappa}_\theta(k)}$. See also section B for a more detailed collection of these standard correspondences.

In principle any function approximator can serve as $\widehat{\kappa}_\theta$, including neural networks, but some model classes make such properties easier to impose than others. In the experiments below, we consider a linear Gaussian basis model to parameterize an exponentially decaying, smooth, isotropic, and real-valued symbol $\widehat{\kappa}_\theta$; see section C for details.

4 Experiments

We evaluate the proposed EFNO on two tasks. First, we consider a simple heat equation whose solution operator is a Gaussian convolution and compare the behaviour of a trained FNO and EFNO when evaluated on different periodic domains. Second, we evaluate the EFNO on a more realistic materials science task and learn the *exchange-correlation potential* across different crystal structures, which inherently requires generalization across both grid sizes and domains.

4.1 Transferring a learned convolution across equivalent periodic cells

This experiment evaluates the abilities of FNO and EFNO to transfer a learned convolution across periodic domains that can represent the same physical system but have different shapes and sizes. To this end, consider the solution operator of the heat equation $\partial_t u = \Delta u$ with periodic boundary conditions, $\mathcal{G}^{(t)} \colon u(0,\cdot) \mapsto u(t,\cdot)$, which is a convolution with symbol $\widehat{\kappa}^{(t)}(k) = \exp(-t|k|^2)$. We fit single FNO and EFNO spectral convolution layers to the exact symbol for a fixed $t = 0.006$ on a small rhombic cell, and then evaluate the fitted operators on an equivalent rectangular cell of twice the area and on $n \times n$ supercells of the fitting cell. Details on the exact experimental setup and the model architectures are provided in section D.1.

Figure 1 shows the results. The FNO shows precisely the domain dependence failure mode described in section 2 and does not transfer the learned convolution from the rhombic cell to the rectangular cell, whereas the EFNO transfers perfectly. Similarly for the $n \times n$ supercells, the relative L_2 error of the FNO grows with the size of the supercell to $\sim 90\%$. The EFNO error remains constant below $10^{-5}\%$, which demonstrates its capabilities to transfer a learned operator across periodic domains.

4.2 Learning exchange-correlation potentials across crystal structures

We now apply the EFNO to a materials science task that requires generalization across both resolutions and domains. The de-facto standard method for simulating the electronic structure of atoms, molecules, and solids is density-functional theory (DFT), but in practice the accuracy of DFT is limited by the accuracy of the *exchange-correlation* (XC) functional. Various XC approximations

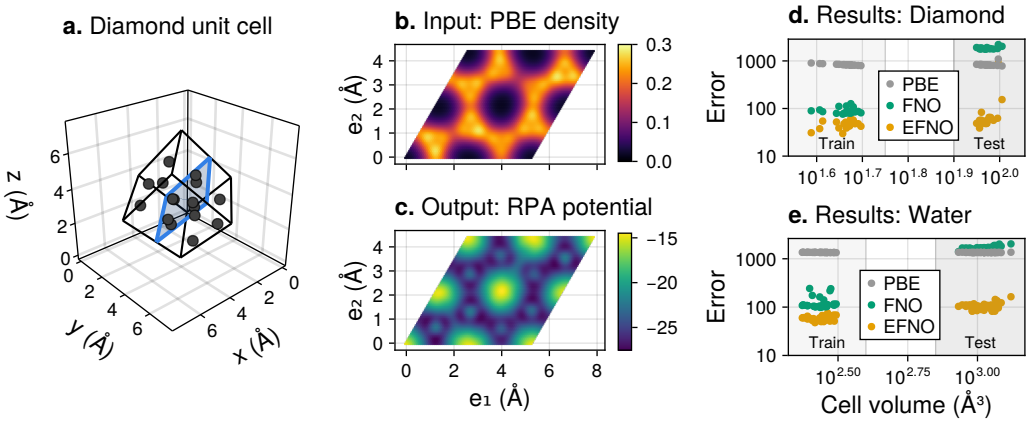

Figure 2: **Overview and results of the exchange-correlation potential learning task. a.** Example system, showing a diamond unit cell with 16 atoms. **b.–c.** PBE electron density and RPA exchange-correlation potential on the slice plane highlighted in (**a.**); these are the inputs and outputs for the operator learning task. **d.–e.** Error (WRMSE) against cell volume for both tasks. The FNO extrapolates poorly from the smaller training cells to the larger test cells; the EFNO generalizes well and achieves errors that are an order of magnitude smaller than the PBE baseline.

have been proposed, ranging from cheap models like the PBE functional [Perdew et al., 1996], to approaches like the random phase approximation (RPA) [Furche, 2001, Fuchs and Gonze, 2002] that are more accurate but are prohibitively expensive for routine use. We consider here the task of learning an operator that maps PBE electron densities to RPA exchange-correlation potentials.

We consider two subsets of the ML-RPA dataset by Riemelmoser et al. [2023] of PBE densities and RPA potentials: *diamond* consisting of 20 8-atom structures and 20 16-atom structures, and *liquid water* consisting of 32 structures of 8 water molecules as well as 39 structures of 31 or 32 water molecules. A visualization of a diamond system and its density and potential is shown in fig. 2. For each subset, we train operators on the smaller structures and evaluate them on the larger ones.

We use the same EFNO architecture for both tasks, consisting of a lifting layer, 2 EFNO layers, and a projection layer, with 8 channels and 16 basis functions. We additionally train a standard FNO with 2 layers, 8 channels, and 4 modes as a baseline, that we apply across cell sizes without modification. We train both models on a gauge-invariant density-weighted mean squared error loss, and evaluate the trained models with the square-root of this metric (WRMSE). More details on the architecture and the training and evaluation procedure are provided in section D.2.1.

Table 1: Density-weighted root mean square error (WRMSE); median value within each split.

	Diamond		Water	
Model	Train	Test	Train	Test
PBE	826.67	825.17	1350.33	1348.37
FNO	81.96	1815.42	108.03	1675.35
EFNO	**47.88**	**56.11**	**57.95**	**103.54**

Table 1 and fig. 2 show the main results. Both the EFNO and FNO are able to fit the training data well and return potentials that are significantly closer to RPA than the PBE baseline. However, the FNO fails to generalize to the larger test structures. The EFNO also shows an increase in test error, but still outperforms PBE by an order of magnitude throughout all instances. More visualizations of the predicted potentials for a few example structures can be found in section D.2.2. Altogether, the results demonstrate that the EFNO is able to learn an operator that generalizes across both grid sizes and domains, showing its potential for applications in materials science and chemistry.

5 Conclusion

We proposed Euclidean Fourier neural operators (EFNOs). By parameterizing the Fourier symbol as a continuous function of the physical wavevector, EFNOs remove the implicit domain dependence of FNOs and learn operators that can be applied consistently across domains of varying shape and

size. This has been demonstrated in experiments on a heat equation and on a materials science task of learning exchange-correlation potentials across crystal structures. Natural extensions of this work include more expressive symbol parameterizations beyond isotropic Gaussian models, comparison to additional baselines, and evaluation on complex PDEs from other fields, to further establish EFNOs as a practical approach to operator learning in the physical sciences.

Acknowledgments and Disclosure of Funding

This research was supported by the Swiss National Science Foundation (SNSF, Grant No. 10002757) as well as the NCCR MARVEL, a National Centre of Competence in Research, funded by the SNSF (Grant No. 205602). We express our gratitude to Stefan Riemelmoser for helpful discussions and to Bruno Ploumhans for feedback on the manuscript.

References

Boris Bonev, Thorsten Kurth, Christian Hundt, Jaideep Pathak, Maximilian Baust, Karthik Kashinath, and Anima Anandkumar. Spherical fourier neural operators: Learning stable dynamics on the sphere. In *International Conference on Machine Learning*, 2023.

Martin Fuchs and Xavier Gonze. Accurate density functionals: approaches using the adiabatic-connection fluctuation-dissipation theorem. *Physical Review B*, 65, 6 2002. doi: 10.1103/physrevb.65.235109. URL `https://doi.org/10.1103/physrevb.65.235109`.

Filipp Furche. Molecular tests of the random phase approximation to the exchange-correlation energy functional. *Physical Review B*, 64, 10 2001. doi: 10.1103/physrevb.64.195120. URL `https://doi.org/10.1103/physrevb.64.195120`.

Yingdi Jin, Xinming Qin, Ruichen Liu, Jie Liu, Zhenyu Li, and Jinlong Yang. V2rho-fno: Fourier neural operator for electronic density prediction. *arXiv preprint arXiv:2603.15669*, 2026.

Seongsu Kim and Sungsoo Ahn. Gaussian plane-wave neural operator for electron density estimation. In *International Conference on Machine Learning*, 2024.

Nikola Kovachki, Zongyi Li, Burigede Liu, Kamyar Azizzadenesheli, Kaushik Bhattacharya, Andrew Stuart, and Anima Anandkumar. Neural operator: Learning maps between function spaces with applications to pdes. *Journal of Machine Learning Research*, 24(89):1–97, 2023.

Jin Lee, Ziming Liu, Xinling Yu, Yixuan Wang, Haewon Jeong, Murphy Yuezhen Niu, and Zheng Zhang. KANO: Kolmogorov–arnold neural operator. In *International Conference on Learning Representations*, 2026. arXiv:2509.16825.

Zhijie Li, Wenhui Peng, Zelong Yuan, and Jianchun Wang. Fourier neural operator approach to large eddy simulation of three-dimensional turbulence. *Theoretical and Applied Mechanics Letters*, 12 (6):100389, 2022. doi: 10.1016/j.taml.2022.100389.

Zongyi Li, Nikola Kovachki, Kamyar Azizzadenesheli, Burigede Liu, Kaushik Bhattacharya, Andrew Stuart, and Anima Anandkumar. Neural operator: Graph kernel network for partial differential equations. *arXiv preprint arXiv:2003.03485*, 2020.

Zongyi Li, Nikola Kovachki, Kamyar Azizzadenesheli, Burigede Liu, Kaushik Bhattacharya, Andrew Stuart, and Anima Anandkumar. Fourier neural operator for parametric partial differential equations. In *International Conference on Learning Representations*, 2021.

Zongyi Li, Daniel Z Huang, Burigede Liu, and Anima Anandkumar. Fourier neural operator with learned deformations for pdes on general geometries. *Journal of Machine Learning Research*, 24 (388):1–26, 2023.

Levi Lingsch, Mike Y Michelis, Emmanuel de Bezenac, Sirani M Perera, Robert K Katzschmann, and Siddhartha Mishra. Beyond regular grids: Fourier-based neural operators on arbitrary domains. In *International Conference on Machine Learning*, 2024.

Ning Liu, Siavash Jafarzadeh, and Yue Yu. Domain agnostic fourier neural operators. In *Advances in Neural Information Processing Systems*, 2023.

Lu Lu, Pengzhan Jin, Guofei Pang, Zhongqiang Zhang, and George Em Karniadakis. Learning nonlinear operators via deeponet based on the universal approximation theorem of operators. *Nature Machine Intelligence*, 3(3):218–229, 2021.

Emmanuel E Oguadimma, Victory C Obieke, and Xueying Yu. Geometry-conditioned fourier neural operators for cubic nonlinear schrödinger dynamics on periodic domains. *arXiv preprint arXiv:2606.27459*, 2026.

Jaideep Pathak, Shashank Subramanian, Peter Harrington, Sanjeev Raja, Ashesh Chattopadhyay, Morteza Mardani, Thorsten Kurth, David Hall, Zongyi Li, Kamyar Azizzadenesheli, Pedram Hassanzadeh, Karthik Kashinath, and Anima Anandkumar. FourCastNet: A global data-driven high-resolution weather model using adaptive Fourier neural operators. *arXiv preprint arXiv:2202.11214*, 2022.

John P. Perdew, Kieron Burke, and Matthias Ernzerhof. Generalized gradient approximation made simple. *Physical Review Letters*, 77(18):3865–3868, 1996. doi: 10.1103/PhysRevLett.77.3865.

Stefan Riemelmoser, Carla Verdi, Merzuk Kaltak, and Georg Kresse. Machine learning density functionals from the random-phase approximation. *Journal of Chemical Theory and Computation*, 19(20):7287–7299, 2023. doi: 10.1021/acs.jctc.3c00848.

Pengqing Shi, Jie Yin, Stephen Tierney, and Junbin Gao. Sirenfno: Efficient and full frequency learning of fourier neural operators. *arXiv preprint arXiv:2606.11518*, 2026.

Jin Young Shin, Jae Yong Lee, and Hyung Ju Hwang. Pseudo-differential neural operator: Generalized fourier neural operator for learning solution operators of partial differential equations. *Transactions on Machine Learning Research*, 2024. arXiv:2201.11967.

Zipeng Xiao, Siqi Kou, Zhongkai Hao, Bokai Lin, and Zhijie Deng. Amortized fourier neural operators. *Advances in Neural Information Processing Systems*, 37:115001–115020, 2024.

Yan Yang, Angela F. Gao, Jorge C. Castellanos, Zachary E. Ross, Kamyar Azizzadenesheli, and Robert W. Clayton. Seismic wave propagation and inversion with neural operators. *The Seismic Record*, 1(3):126–134, 2021. doi: 10.1785/0320210026.

Zhiwei Zhao, Changqing Liu, Yingguang Li, Zhibin Chen, and Xu Liu. Diffeomorphism neural operator for various domains and parameters of partial differential equations. *Communications Physics*, 8, 2025. doi: 10.1038/s42005-024-01911-3.

A Related work

Neural operators on varying geometries. Fourier neural operators [Li et al., 2021] apply learned per-mode weight matrices to truncated Fourier coefficients, within the general operator-learning framework of Kovachki et al. [2023]. Several variants extend them to irregular or varying geometry by deforming the domain to a regular grid (Geo-FNO, Li et al., 2023), mapping it to a fixed reference domain (DNO, Zhao et al., 2025), encoding it with a smoothed characteristic function (DAFNO, Liu et al., 2023), replacing the FFT with a non-uniform transform [Lingsch et al., 2024], or supplying the domain geometry as an extra input channel [Oguadimma et al., 2026]; in each case the spectral weights stay indexed by mode number, so transferring across physical domains still requires re-fitting or re-learning them. Non-spectral operators such as DeepONet [Lu et al., 2021] and graph neural operators [Li et al., 2020] handle varying geometry natively through query coordinates or message passing, respectively, but forgo the FFT and its efficiency.

Learned continuous spectral symbols. A closer line of work replaces the discrete weight table with a function of the frequency variable. AM-FNO [Xiao et al., 2024] and SirenFNO [Shi et al., 2026] learn a network over the mode number (or a grid-normalized version of it), covering all modes with a fixed parameter budget. PDNO [Shin et al., 2024] and KANO [Lee et al., 2026] instead read the weight as a pseudo-differential symbol that also depends on position, for variable-coefficient

problems. PDNO formulates its symbol over $\xi \in \mathbb{R}^d$ but restricts the symbol network to integer modes $\xi \in \mathbb{Z}^d$ (their Appendix B2), a choice they motivate by continuity of the operator. In all of these the frequency argument is the mode number, so the represented operator depends on the domain, and the weights are trained and evaluated at a single physical scale. Our layer keeps a position-independent convolution but takes the physical wavevector as the argument (table 2).

Table 2: Parameterization of the spectral weight across FNO variants. FNO stores a discrete table over modes; the others learn it as a function. Its argument is the mode number, with PDNO and KANO adding the position (a pseudo-differential symbol); EFNO alone uses the physical wavevector, the quantity that changes with the domain.

Method	Spectral weight	Kernel argument
FNO [Li et al., 2021]	lookup table	mode number
AM-FNO [Xiao et al., 2024]	learned function	mode number
SirenFNO [Shi et al., 2026]	learned function	mode number
PDNO [Shin et al., 2024]	learned function	mode number & position
KANO [Lee et al., 2026]	learned function	mode number & position
EFNO (ours)	learned function	physical wavevector

Applications to electronic structure. Closest to our application are neural operators that predict electronic-structure fields. V2Rho-FNO [Jin et al., 2026] maps the external potential to the electron density for molecules in a fixed cubic box, and GPWNO [Kim and Ahn, 2024] predicts electron densities across crystals using a combined orbital and plane-wave basis; in both cases the spectral weights are tied to a single domain or bypass the Fourier-multiplier structure. Our experiment learns a related map on structures whose lattices differ from sample to sample.

B Kernel properties

Table 3 collects some standard correspondences from Fourier analysis connecting the real-space convolution kernel and its Fourier transform.

Table 3: Correspondence between real-space and spectral properties of the kernel. Each row is an equivalence.

Real-space kernel κ	Spectral kernel $\widehat{\kappa}$
Real-valuedness κ real-valued	*Hermitian symmetry* $\widehat{\kappa}(-k) = \overline{\widehat{\kappa}(k)}$
Smoothness κ has s derivatives in L^2	*Decay at large* $\lvert k\rvert$ $\lvert k\rvert^s\, \widehat{\kappa} \in L^2$
Range κ supported in $\lvert x\rvert \le R$	*Smoothness of* $\widehat{\kappa}$ $\widehat{\kappa}$ entire, $\lvert\widehat{\kappa}(k)\rvert \lesssim e^{R\lvert \mathrm{Im}\, k\rvert}$
Isotropy $\kappa(x) = \kappa(\lvert x\rvert)$	*Isotropy* $\widehat{\kappa}(k) = \widehat{\kappa}(\lvert k\rvert)$

C Gaussian basis parameterization of the EFNO symbol

We parameterize the symbol $\widehat{\kappa}_\theta$ as a linear combination of Gaussian basis functions in $|k|^2$,

$$\widehat{\kappa}_\theta(k) = \sum_{j=1}^{n_{\text{basis}}} \phi_j\big(|k|^2\big)\; w_j, \qquad \phi_j\big(|k|^2\big) = \exp\!\left(\frac{-(|k|^2 - \mu_j)^2}{2\sigma^2}\right), \tag{5}$$

with n_{basis} centers μ_j placed uniformly on $[0, k_{\text{max}}^2]$ in $|k|^2$, a shared width $\sigma = k_{\text{max}}^2/n_{\text{basis}}$, and trainable real coefficients $w_j \in \mathbb{R}^{c\times c}$. Since the basis is Gaussian in $|k|^2$, the symbol $\widehat{\kappa}_\theta(k)$ is a

smooth function of k, decays as $|k| \to \infty$, is isotropic as it depends only on $|k|$, and is real-valued by construction; see section B for the correspondences between these properties and those of the real-space kernel.

D Additional experiment details and results

D.1 Experiment 1: Gaussian smoothing across periodic cells

Operator and cells. The test operator is the solution operator of the heat equation $\partial_t u = \Delta u$ with periodic boundary conditions, $\mathcal{G}^{(t)} \colon u(0,\cdot) \mapsto u(t,\cdot)$ at $t = 0.006$, a convolution with the known symbol $\widehat{\kappa}^{(t)}(k) = \exp\bigl(-t\,|k|^2\bigr)$. Both models are fitted on a rhombic cell with lattice

$$L_{\text{fit}} = \begin{pmatrix} \sqrt{3}/2 & \sqrt{3}/2 \\ 1/2 & -1/2 \end{pmatrix}, \tag{6}$$

sampled on a 48×48 grid. Models are then evaluated on two different sets of test cells:

(i) a rectangular cell of twice the area, $L_{\text{rect}} = \begin{pmatrix} \sqrt{3} & 0 \\ 0 & 1 \end{pmatrix}$, on an 84×48 grid;

(ii) $n \times n$ supercells with lattice $L_n = nL_{\text{fit}}$, for $n = 1, \ldots, 6$, on $48n \times 48n$ grids, holding the resolution per unit length constant.

With this choice, any field that is periodic on L_{fit} is also periodic on L_{rect} and on L_n for all n.

Models and fitting. Both evaluated models consist only of a single spectral convolution layer so that the only difference is the parameterization of the symbol. The FNO keeps $M = 12$ modes per dimension (325 weights); The EFNO uses the Gaussian basis of eq. (5) with $n_{\text{basis}} = 25$ coefficients, centers uniform on $[0, k_{\text{max}}^2]$ with $k_{\text{max}}^2 = -\log\bigl(10^{-6}\bigr)/t$ and width $\sigma = k_{\text{max}}^2/n_{\text{basis}}$. Both are fitted in closed form to the exact symbol on the fitting cell's wavevector grid, with no input-output data and no iterative optimisation: the FNO sets $R_m = \widehat{\kappa}(k_m)$ directly, the EFNO solves a least-squares problem with a small Tikhonov term ($10^{-10}\,\mathrm{tr}(\Phi^\top \Phi)/n_{\text{basis}}\, I$) for numerical conditioning.

Input field and evaluation. The probe is a periodic array of Gaussian sources (width 0.03, one per lattice site, summed over periodic images). As it has the periodicity of the rhombic fitting cell, it is exactly representable on every supercell. Errors are relative L_2 against the exact smoothed field, in percent.

Results. Table 4 reports the error on the fitting cell, the rectangular supercell, and the $n \times n$ supercells. Figure 1 visualises the rectangular-cell transfer and the supercell sweep. On the fitting cell, both models are near-exact. On both the rectangular test cell and the $n \times n$ supercells, the FNO error becomes large while the EFNO error remains constant at the fitting residual.

Table 4: Relative L_2 error (%) of the FNO and EFNO. The FNO is near-exact on the fitting cell but fails to transfer; the EFNO stays at its basis-approximation residual on every cell.

	Single cell		$n \times n$ supercell				
Model	Fitting	Rectangular	$n = 2$	$n = 3$	$n = 4$	$n = 5$	$n = 6$
FNO	~ 0	49.70	66.09	85.16	89.60	90.12	90.16
EFNO	3.5×10^{-6}	3.5×10^{-6}	3.5×10^{-6}	3.5×10^{-6}	3.5×10^{-6}	3.5×10^{-6}	3.5×10^{-6}

D.2 Experiment 2: Exchange-correlation potential learning

D.2.1 Architecture and training

Dataset and splits. We use the ML-RPA dataset [Riemelmoser et al., 2023], consisting of 189 crystal structures spanning small molecules, diamond bulk systems, surfaces, and liquid water. We consider two subsets: the *diamond* subset, consisting of 20 eight-atom structures for training and

validation, and 20 sixteen-atom structures for testing; and the *liquid-water* subset, consisting of 32 structures of eight water molecules for training and validation, and 39 structures of 31 or 32 water molecules for testing. In both cases, we train on the smaller structures and test on the larger ones, with an 80/20 train/validation split. The training and validation structures are Fourier-resampled to a common grid (48^3 for diamond, 80^3 for water) to enable efficient batching during training; the test structures are kept on their original grids, so that the evaluation reflects generalization across both grid sizes and domains.

Loss and evaluation metric. Following Riemelmoser et al. [2023], we train the models on a gauge-invariant density-weighted mean squared error loss,

$$\mathcal{L} = \frac{1}{N_e} \int_\Omega \rho(r) \left(\tilde{v}_{\text{xc}}^{\text{pred}}(r) - \tilde{v}_{\text{xc}}^{\text{ref}}(r) \right)^2 \mathrm{d}r, \tag{7}$$

where $N_e = \int_\Omega \rho(r)\mathrm{d}r$ is the number of electrons in the cell Ω, and $\tilde{v}_{\text{xc}} = v_{\text{xc}} - \frac{1}{N_e} \int_\Omega \rho(r)\, v_{\text{xc}}(r)\mathrm{d}r$ subtracts the density-weighted mean to remove the constant gauge freedom of v_{xc}. All integrals are discretized over the uniform real-space grid. We train on the mean of $\mathcal{L}$ over the training structures, and report its square root (WRMSE), averaged over structures, in meV/e^-.

Model and training. Each model consists of a lifting layer that maps the scalar input to c channels, two (E)FNO blocks, and a projection layer that maps back to a single channel. As in the standard FNO, each block is a sum of a spectral convolution and a pointwise linear channel-mixing layer, followed by a `gelu` activation. Both models use $c = 8$ channels, two (E)FNO layers, a lifting and a projection layer. The EFNO uses 16 basis functions per layer, spread uniformly in $[0, k_{\text{max}}^2]$ with $k_{\text{max}}^2 = 40$ bohr^{-2}, chosen to cover the ML-RPA dataset's plane-wave band limit (set to $E_{\text{cut}} = 600$ eV throughout). The FNO baseline uses 4 modes per layer. Both models are trained with Adam at a constant learning rate of 10^{-2}, full-batch over all training structures, for a fixed number of steps, and we select the checkpoint with the lowest validation WRMSE.

D.2.2 Visualizations of the predicted potentials

Figures 3 and 4 show the predicted RPA exchange-correlation potentials for one representative training and one representative test structure from each task (diamond and liquid water), with the PBE electron density as input. On the training structures both models reproduce the RPA potential; on the test structures the FNO error grows substantially while the EFNO stays close to the reference, which is consistent with the aggregated results of table 1.

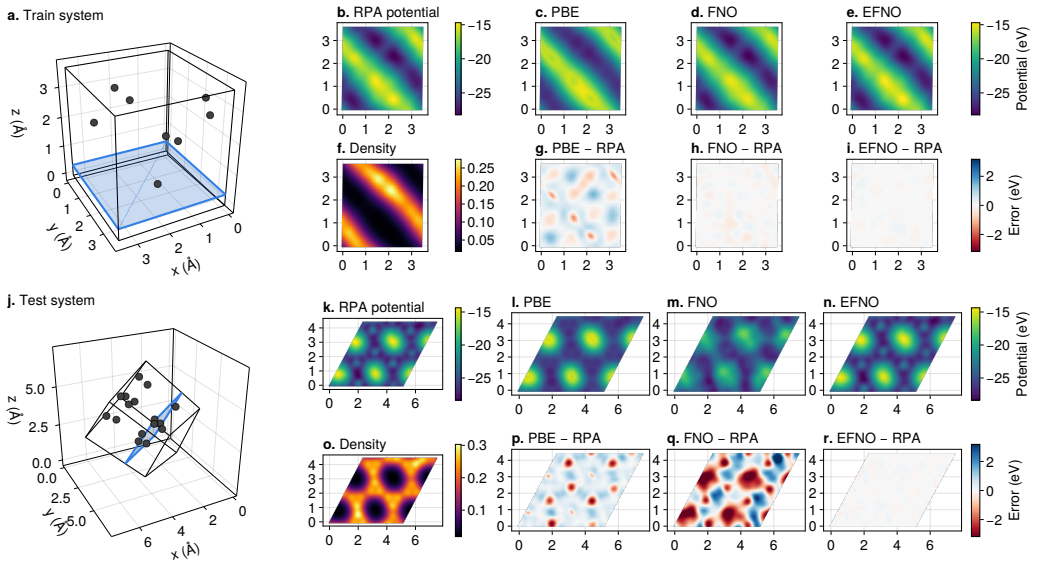

Figure 3: **Predicted potentials for a representative diamond train and test structure. a.** Unit cell of a training system, showing the plane along which the density and potential are visualized. **b.** RPA reference potential. **c.–e.** PBE, FNO, and EFNO predictions. **f.** Input electron density (PBE). **g.–i.** Difference of each prediction to the reference. **j.–r.** Corresponding panels showing the cell, potentials, density, and errors for a test system. On the training system, both the FNO and the EFNO are able to reproduce the RPA potential well and show small errors (**h.–i.**). On the test system, the FNO shows substantial errors (**q.**) that are larger than the PBE baseline (**p.**), while the EFNO stays close to the reference (**r.**).

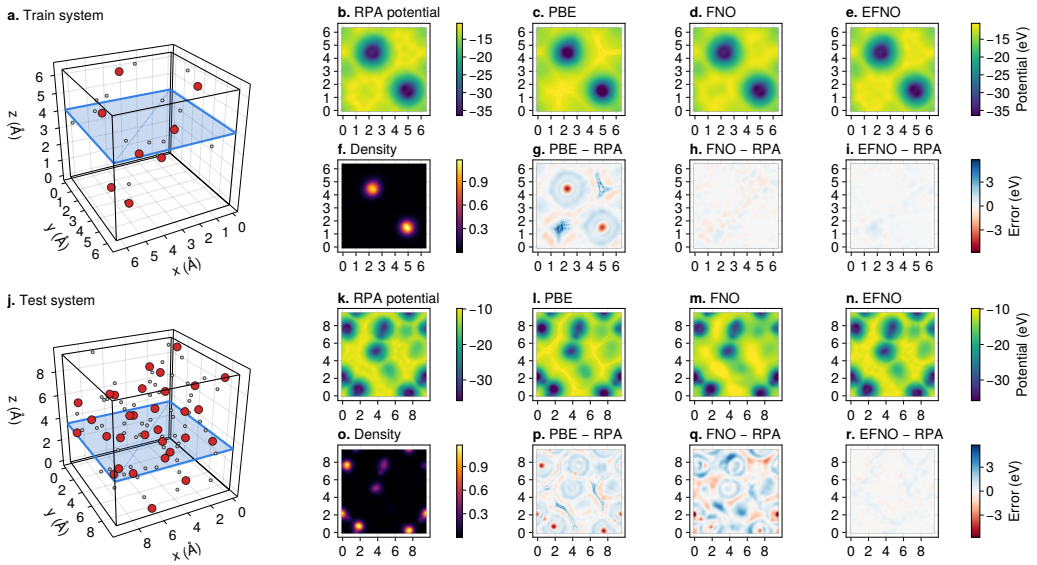

Figure 4: **Predicted potentials for a representative liquid-water train and test structure. a.** Unit cell of a training system, showing the plane along which the density and potential are visualized. **b.** RPA reference potential. **c.–e.** PBE, FNO, and EFNO predictions. **f.** Input electron density (PBE). **g.–i.** Difference of each prediction to the reference. **j.–r.** Corresponding panels showing the cell, potentials, density, and errors for a test system. On the training system, both the FNO and the EFNO are able to reproduce the RPA potential well and show small errors (**h.–i.**). On the test system, the FNO shows substantial errors (**q.**) that are larger than the PBE baseline (**p.**), while the EFNO stays close to the reference (**r.**).